Ultra-Wideband, Directive and Circular Polarization Lens Antennas for Future Communications

R. A. dos Santos, G. L. S. Fré, D. H. Spadoti

***Abstract*—This paper presents a potential featured antenna for future wireless communication networks. The use of a hemispherical dielectric lens combined with an equiangular spiral printed antenna is proposed to achieve a radiator design with high-gain, operating in a frequency range between 8.0 GHz to 15.6 GHz in circular polarization. Numerical analyses performed by the ANSYS HFSS software, and experimental measurements validated the functionality of the proposed structure, reaching gains greater than 14.2 dBi.**

***Index Terms*—Circular polarization, equiangular spiral antenna, high gain, lens antennas, ultrawideband.**

I. Introduction

In the last decades, both the numbers of mobile communications users and data transmission traffic are exponentially increasing. Millimeter and submillimeter waves are being utilized by the modern fifth-generation (5G) mobile systems in order to offer the desired high data throughput and broadband operation [1]. A key component to develop the broadband system is the choice of a correct radiator element. In this scenario, printed equiangular spiral antenna (PESA) is opening a new interesting solution for broadband systems, due to their unique features, such as: low profile, easy manufacture, light weight, and low cost [2-4]. However, for compensating the path propagation losses, high data rates traffic requires high-gain antennas, but due to the intrinsic absence of a ground plane, PESA presents a low-gain bidirectional radiation pattern [5-6]. To overcome such limitations, R.A. Santos, et al. [7] proposed a dielectric lens integrated with a broadband high-directivity ultra-wideband beamsteering antenna array designed by a set of different printed antennas achieving 13 dBi gain with bandwidth of 40% [7]. G.H. Lee, et al. [8], proposed a dual-bowtie antenna loaded with a double-sided dielectric lens, presenting a gain of 15.1 dBi and a bandwidth of 64.5% [8]. Two orthogonal Vivaldi antennas (forming a cross-shaped configuration to excite linear (horizontal/vertical) and circular polarization) loaded with a spherical-axicon dielectric lens were presented in [9] for 'wideband and high-gain performance getting 15.8 dBi of gain and 160% of bandwidth.

In this paper, an ultra-wideband, directive and circular polarized equiangular spiral antenna loaded with a hemispherical dielectric lens is presented (Fig. 1). The proposed design presents, at the same time, high gain in a large broadband operation (8.0 GHz to 15.6 GHz), for circular polarization features, being interesting for modern telecommunications systems, alleviating polarization mismatches and multipath losses [10].

This paper is organized into four sections. In Section II, ultra-wideband printed spiral antenna theoretical design is presented. In Section III, the analysis of the proposed antennas is presented. Finally, conclusions are presented in Section VI.

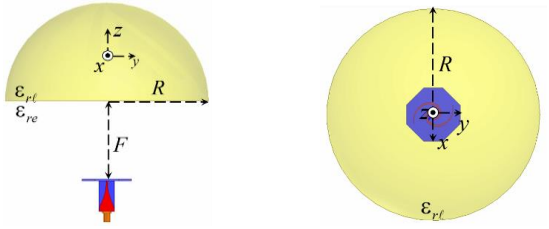

(a) (b)

Fig. 1. Ultra-wideband, directive and circular polarization lens antenna. Side view, (b) Upper view.

II. Ultra-Wideband Printed Spiral Antenna

The ultra-wideband printed spiral antenna belongs to a radiator class that can operate in a wide bandwidth, which are defined as frequency independent antennas [11-12], since the antenna input impedance is practically constant within its entire bandwidth. Typically, this kind of radiator has an imaginary impedance (X_{in}) close to zero ohms, whereas the real part (R_{in}) is over one-hundred ohms. Thus, impedance matching systems need to be included, given the higher Rin, values. This is incompatible with 50 Ω radiofrequency telecommunication standards for measurement equipment. For this reason, an Ultra-Wideband Printed Spiral Antenna was designed in two steps: the antenna structure (section 2.1) and the wideband

R. A. dos Santos is with the Faculty of Electrical Engineering, Federal University of Uberlândia - UFU, Brazil, e-mail: renans@ufu.br, https://orcid.org/0000-0002-7219-0953.

D. H. Spadoti is with the Telecommunication's Lab (LabTel), Federal University of Itajubá – UNIFEI, Brazil, e-mail: spadoti@unifei.edu.br, https://orcid.org/0000-0001-5698-6639.

G. L. S. Fré is with the Flextronics Institute of Technology Product Inovation Center Sorocaba-SP, Brazil, e-mail: gabriel.fre@fit-tecnologia.org.br, https://orcid.org/0000-0002-7719-3715.

DOI: 10.14209/jcis.2023.7

impedance matching structure (section 2.2).

A. *Equiangular Spiral Antenna Design*

The equiangular spiral antenna comprises two arms rotated at 180º relative to each other (see Fig. 2). Each spiral arm is defined by a set of three angular functions of α, where α is the angle of rotation measured from the x axis as in Fig. 2(a), resulting in three segment curves. The external curve is given in [13]:

$$\begin{aligned} r_1(\alpha) &= e^{a(\alpha+\delta)} \\ r_{1x}(\alpha) &= e^{a(\alpha+\delta)}\cos(\alpha) \\ r_{1y}(\alpha) &= e^{a(\alpha+\delta)}\cos(\alpha) \end{aligned}, 0 \le \alpha \le \alpha_{máx}, \quad (1)$$

where a is the radial expansion rate, and δ is a factor connected to the initial radius r_0, and the value given in [13]:

$$\delta = \frac{1}{a}\ell n(r_0) \quad (2)$$

Thus, the external curve segment is given in (1), which is defined as being between $0 < \alpha < \alpha_{máx}$. The maximum α gives the total length of each spiral $S(\alpha_{máx})$, thus [13]:

$$S(\alpha_{máx}) = \left(r(\alpha_{máx}) - r_0\right)\sqrt{1+\frac{1}{a^2}} \quad (3)$$

For equiangular spiral antenna designs, the total spiral length must be equal to the wavelength, so that $S(\alpha_{máx}) = \lambda_g$ (as the equiangular spiral antenna does not have a ground plane, λ_g is defined as the guided wavelength, resulting from the mean value between the vacuum and dielectric laminate) defining $\alpha_{máx}$ as follows:

$$\alpha_{máx} = \frac{1}{a}\ell n\left(\frac{\lambda_g}{r_0\sqrt{1+a^2}}+1\right) - \delta \quad (4)$$

Each internal edge of each spiral arm is set by curvilinear sections, with the first spiral given by the same expansion rate as the external curve, but with a different initial radius. This factor is δ', giving the curve in:

$$\begin{aligned} r_2(\alpha) &= e^{a(\alpha+\delta')} \\ r_{2x}(\alpha) &= e^{a(\alpha+\delta')}\cos(\alpha) \\ r_{2y}(\alpha) &= e^{a(\alpha+\delta')}\operatorname{sen}(\alpha) \end{aligned}, 0 \le \alpha \le (\alpha_{máx} - \pi), \quad (5)$$

defining δ' in,

$$\delta' = \frac{1}{a}\ell n(r_0 - b) \quad (6)$$

where b is the initial distance between both the external and internal curves. For our structure:

$$b = r_1(0) - r_2(0) \cong 0.25 r_0 \quad (7)$$

The first internal curve is the result of (5) for the range $0 < \alpha < (\alpha_{máx} - \pi)$ [13]. Hence, this curve connects both previously defined equations, requiring a different expansion rate a', and the initial radius factor, δ". Thus:

$$\begin{aligned} r_3(\alpha) &= e^{a'(\alpha+\delta'')} \\ r_{3x}(\alpha) &= e^{a'(\alpha+\delta'')}\cos(\alpha) \\ r_{3y}(\alpha) &= e^{a'(\alpha+\delta'')}\operatorname{sen}(\alpha) \end{aligned}, (\alpha_{máx} - \pi) \le \alpha \le \alpha_{máx}. \quad (8)$$

where δ" is given in [13]:

$$\delta'' = \frac{\pi\delta + \alpha_{máx}(\delta' - \delta)}{\delta - \delta' + \pi} \quad (9)$$

and a' is described by:

$$a' = \frac{a(\alpha_{máx} + \delta)}{\alpha_{máx} + \delta''} \quad (10)$$

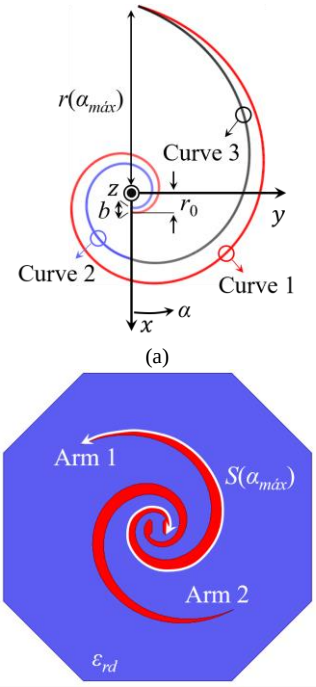

Fig. 2. Equiangular Spiral Antenna. (a) Arm formation, (b) Final structure.

The material chosen for the equiangular spiral antenna design was dielectric laminate Arlon DiClad 880, with relative electric permittivity ε_{rd} = 2.2, and 1.52 mm thickness. The design frequency is 4 GHz, yielding a guided wavelength of 59.25 mm. The value of the initial radius was set equal to the dielectric plate thickness, r_0 = 1.52 mm, thus the width of each a spiral arm conductor strip is b equal 0.38 mm. The initial radius was set equal to the dielectric plate thickness to facilitate the insertion of the impedance matching and balance systems, so that each of the conducting lines from the transformer would fit into the lines on the spiral.

To make equiangular spiral feeding easier, a contact base at the beginning of each arm was created (see Fig. 2(b)). This base geometry does not greatly influence antenna operation. However, an initial distance between the arms equal to the dielectric laminate thickness was defined, making it easier to insert impedance balance and matching.

It should be noted that all variables are influenced by the

radial expansion rate. We have numerically evaluated a efficiency for antenna operation, by applying the finite element method in the HFSS software. The analysis used a range from 3.5 GHz to 18.5 GHz.

The equiangular spiral antenna performance was evaluated for expansion rates between 0.15 and 0.35 (see Fig. 3). We investigated the real part of the input impedance (R_{in}) (see Fig. 3(a)), the imaginary part of the input impedance (X_{in}) (see Fig. 3(b)), and the axial ratio (AR) (see Fig. 3(c)).

The real part of the input impedance, R_{in}, reached values above 100 Ω from the projected frequency (see Fig. 3(a)). Each radial expansion rate value leads to impedance convergence at a value of R_{in} with a frequency increase. We observed R_{in} at 150 Ω when $0.2 < a < 0.3$.

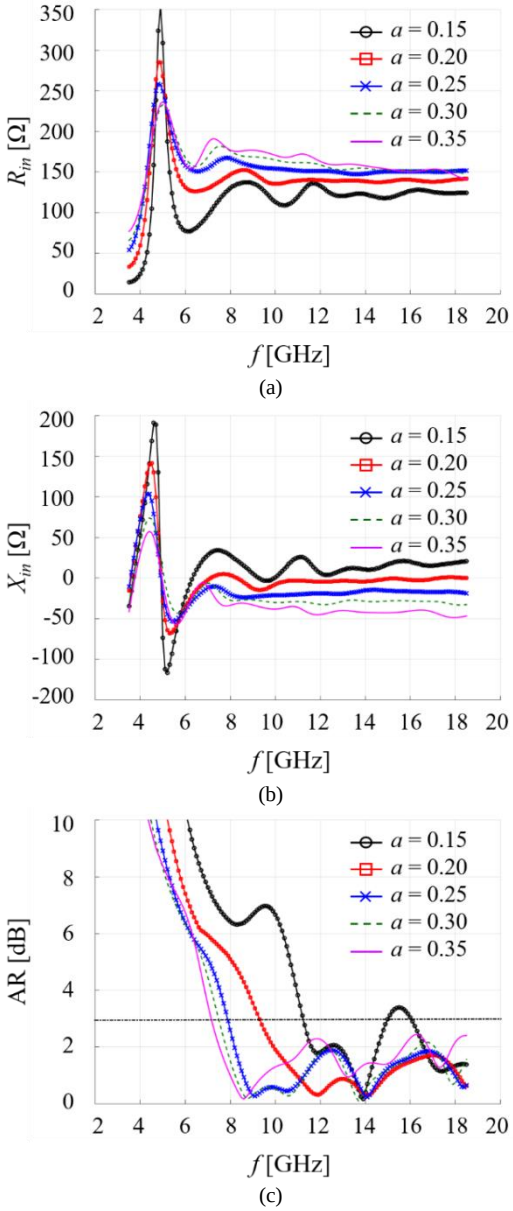

Fig. 3. Frequency response of the equiangular spiral antenna. (a) Real part of the input impedance, (b) Imaginary part of the input impedance, (c) Axial ratio.

The imaginary part of the input impedance performed similarly to the real part (see Fig.3 (b)). However, the impedance values were kept close to zero ohms. Increasing 'a', X_{in} values decreased, and for $a < 0.2$ inductive reactance was observed, while for $a > 0.2$ capacitive reactance was observed.

The axial ratio shows the antenna polarization performance. For circular polarization, the bandwidth can be expressed for frequency ranges where AR values are less than 3dB. Thus, the equiangular spiral antenna showed AR < 3dB for large bandwidths (see Fig. 3(c)). It is important to emphasize that AR < 3dB tends to start at frequencies greater than twice the design frequency [13]. For the equiangular spiral antenna, the total arm length is small if compared with the wavelength, and the radiated field is linearly polarized. As the frequency increases, the wave becomes elliptically polarized, until it reaches the circular polarization. However, when increasing the radial expansion rate, AR < 3dB values started at lower frequencies. Thus, the radial expansion rate was defined as $a = 0.25$, starting at 8 GHz with *Rin* and X_{in} being almost constant, at 150 Ω and 0 Ω, respectively. Thereby, the final equiangular spiral antenna dimensions are $\delta = -25.96$ radians, $\alpha_{máx} = 9.39$ radians, $\delta' = -27.1$ radians, $\delta'' = -21.51$ radians, and $a' = 0.34$.

B. Impedance Matching and Balance System for Ultra-Wideband Radiators

Beyond Rin being higher than 100 Ω, another intrinsic characteristic of the equiangular spiral antenna is that excitation currents should be 180° out-of-phase, i.e., balanced excitation. Thus, beyond the impedance transform, system balance feeding needs to be implemented. In this study we propose an impedance transformer design that transforms a 50 Ω microstrip line into a parallel symmetric line with impedance greater than 100 Ω (see Fig. 4).

The design of the impedance matching and balance system comprised two parts: width reduction for the microstrip line, increasing the impedance value, and ground plane transformation into a symmetric parallel line.

For operation in large bandwidths, the impedance transform must also be wideband. One way to obtain this is by applying successive transmission line stages (each one with its respective characteristic impedance) set in cascade. We used the Tschebyscheff polynomial method [14] to specify the width for each segment of the transmission line, so the reflection coefficient (Γ) was not affected. Each transforming length n must be ℓ_{Tn}, long, equal to one-quarter the guide wave.

The transmission line stages are detailed in Fig. 4(a) and Table 1. Four impedance transformer stages were designed with Arlon DiClad 880 dielectric laminate material (with relative dielectric permittivity $\varepsilon_{rd} = 2.2$ and thickness at 1.52 mm). The transform started after the microstrip line at 50 Ω, with width $w_1 = 3.87$ mm, and length $\ell_1 = 5.5$ 2mm. The initial ground plane width was defined as $w_g =$ 13.54 5mm. The final impedance of the transformer was defined at 120 Ω. Thus, the reflection coefficient is −19 dB, considering antenna impedance at 150 Ω. Additionally, the final transmission line width for the prototypes after the transformers is $w_2 = 1$ mm.

In the bottom part of the transformer and balance impedance (see Fig. 4(b)), a smooth transition width was included, minimizing the undesirable effects for the reflection coefficient,

thereby avoiding changes to the impedance characteristics at the input and output connectors, since the reflected wave percentage was reduced. This performance was obtained using two Gaussian functions, as follows:

$$w_g(\ell_{Ti}) = \frac{1}{2}\left[w_g g_1(\ell_{Ti}) + w_2 g_2(\ell_{Ti})\right] \quad (11)$$

The bottom width of the conductor was defined along its length ℓ_{Ti} by compounding two Gaussian functions ($g_1(\ell_{Ti})$ and $g_2(\ell_{Ti})$) with different variances.

TABLE I. SIZING THE IMPEDANCE TRANSFORMER.

Transformer section	w_{Tn} [mm]	Z_{Tn} [Ω]	ℓ_{Tn} [mm]	Γ_n [dB]
1	3.21	65	5.44	-17.54
2	2.21	80	5.50	-19.67
3	1.57	95	5.56	-21.31
4	1.00	120	5.63	-18.65

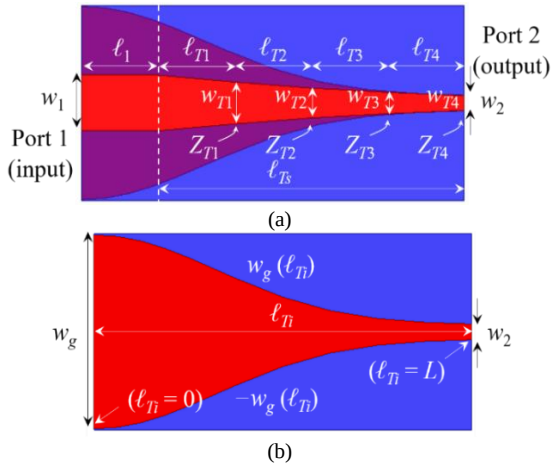

Fig. 4. Impedance transformer. (a) Upper view, (b) Bottom view.

The first Gaussian function, $g_1(\ell_{Ti})$, must give averages equal to zero, taking the maximum value of the function as the input line, expressed in:

$$g_1(\ell_{Ti}) = e^{-\left(\frac{(\ell_{Ti})^2}{2\sigma_1^2}\right)} \quad (12)$$

where variance σ_1^2 is the respective variance.

The second Gaussian function, $g_2(\ell_{Ti})$, must present averages equal to the total length (L) of the line so the maximum value of the function occurs at the extremity of the line. The $g_2(\ell_{Ti})$ is given in:

$$g_2(\ell_{Ti}) = e^{-\left(\frac{(\ell_{Ti}-L)^2}{2\sigma_2^2}\right)} \quad (13)$$

where variance σ_2^2 is the respective variance.

The Gaussian functions have a maximum value equal to 1, therefore, $g_1(\ell_{Ti})$ and $g_2(\ell_{Ti})$ must be multiplied by w_g and w_2 respectively. Variances σ_1^2 and σ_2^2 were determined from numerical analyses performed in the ANSYS HFSS software, and the best results were $\sigma_1 = L/3$ and $\sigma_2 = L/12$.

The efficiency of the impedance matching and balance system were validated numerically in the ANSYS HFSS software. We analyzed the transformer impedance (R_T) (see Fig 5(a)) and the S-parameters (see Fig 5(b)). Fig. 5(a) shows that the real part of transformer input and output impedances vary around 50 Ω and 150 Ω, respectively, all along the frequency range. Fig. 5(b) shows the performance of the reflection and transmission coefficients. The input and output impedance were 50 Ω and 150 Ω, respectively, and S_{11} was kept below −15.6 dB and S_{21} greater than −1.6dB, thus, the structure performed with low losses and low reflectivity.

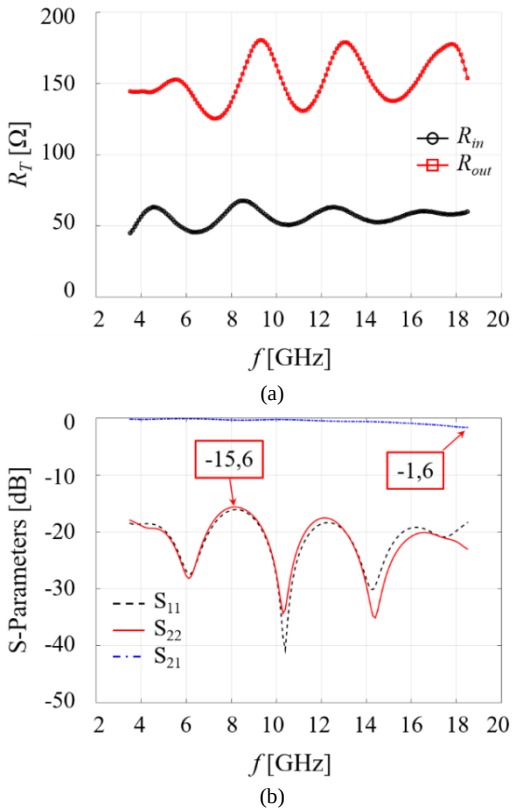

Fig. 5. Frequency response of the impedance transformer. (a) Real impedance part (b) S-parameters.

C. Equiangular Spiral Antenna with an Impedance Matching and Balance System

After designing the equiangular spiral antenna and the impedance matching and balance system independently, we then analyzed the structures together. The antenna reflection coefficient with the transformer is shown in Fig 6. Note that S_{11} undergoes a significant change, so that the bandwidth $S_{11} <$ −10 dB goes from 3.7 GHz to 17.9 GHz.

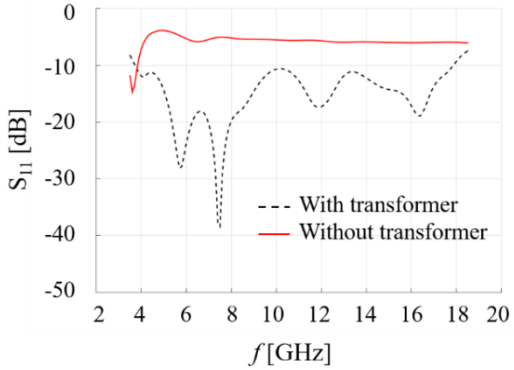

Fig. 6. Performance of the reflection coefficient of the equiangular spiral antenna.

III. Ultra-wideband, Directive and Circular Polarization Lens Antenna Design

To achieve high gain and directivity, a hemispherical dielectric lens was coupled to the ultra-wideband circular polarization printed spiral antenna (see Fig. 7). The setup included a wooden base (brown), with dielectric constant and a dissipation factor at $\varepsilon_{rw} = 1.22$ and $\tan(\delta)_w = 0.1$, respectively [15]. The lens fasteners for positioning the PLA material illuminators (gray) were $\varepsilon_{rs} = 3.5$ and $\tan(\delta)_s = 0.07$ [16].

Two dimensions are extremely important for hemispherical dielectric lens designs, the radius R, and the inserted illuminator distance F (see Fig. 7(b)). So, the lens functions correctly as an electromagnetic wave collimator, the F distance is [17]:

$$F \cong \left(\frac{\sqrt{\varepsilon_{re}}}{\sqrt{\varepsilon_{r\ell}} - \sqrt{\varepsilon_{re}}} - 1 \right) R \qquad (14)$$

where ε_{re} and $\varepsilon_{r\ell}$ are the dielectric relativity in external media and the lens material, respectively. Polytetraflourethylene (PTFE) (at $\varepsilon_{r\ell} = 2.2$) was used for the lens material. We set R equal to $3\lambda_0$ at 10 GHz, where λ_0 is the free space wavelength, given the constructive limitations, resulting in an F distance equal to 71.37 mm. To fix the lens on the PLA support, we designed a PTFE hollow cylindrical extension (see Fig. 7(c) and (d)), with d_s = 20 mm, and t_s = 10 mm, and then built a prototype to conduct measurements (see Fig. 8).

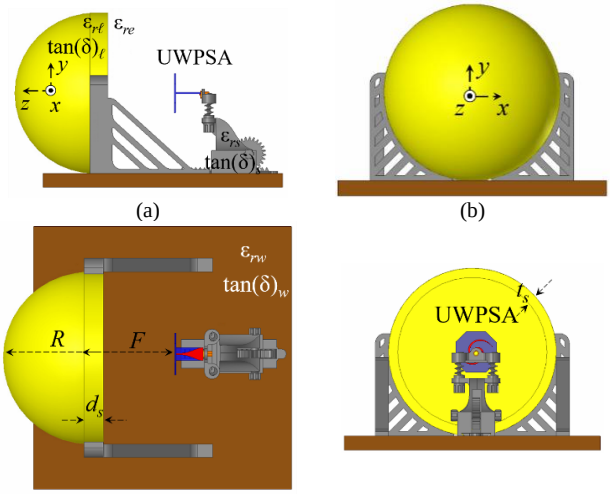

Fig. 7. Ultra-wideband, directive and circular polarization lens antenna numerical model. (a) Side view, (b) Front view, (c) Upper view, (d) Back view.

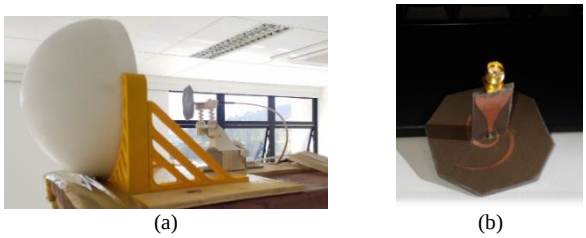

Fig. 8. Ultra-wideband, directive and circular polarization lens antenna prototype. (a) Lens antenna, (b) Equiangular spiral antenna.

Resonance can occur in the dielectric lens with dimensions in the order of λ_0 [17]. This is an undesirable effect and limits the functionality of the system. Therefore, 8 GHz was defined as the initial frequency for operating the proposed antenna.

A. Reflection coefficient

The numerical and measured reflection coefficients, S_{11}, were investigated and are compared in Fig. 9. For frequencies above 15 GHz the S_{11} showed considerable variation, mainly due to imperfections in the manufacturing process of the illuminator prototype, with more influence for higher frequencies. However, the antenna showed bandwidths up to 15.6 GHz.

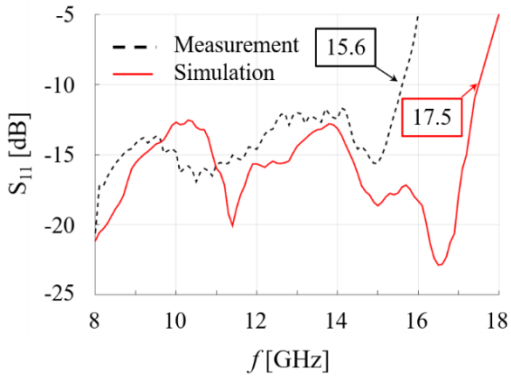

Fig. 9. Ultra-wideband, directive and circular polarization lens antenna reflection coefficients.

B. Radiation Performance

Given the practical limitations, the gain and radiation pattern measured were performed up to 10GHz. Fig. 10 presents the gain vs frequency curves in the direction of maximum radiation, highlighting that the simulations show that the gain can reach 18dBi in the operating range. The simulated and measured radiation patterns are shown in Fig. 10 for frequencies between 8.0 GHz and 10 GHz, showing very precise responses. The results were compared in co-polarization (Co-pol) and cross-polarization (X-pol) to verify functionality in circular polarization. Table 2 shows the gain values in the direction of maximum radiation, proving the functionality of the proposed structure.

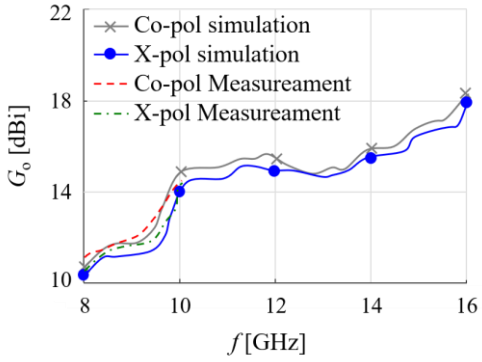

Fig. 10. Ultra-wideband, directive and circular polarization lens antenna gain vs frequency.

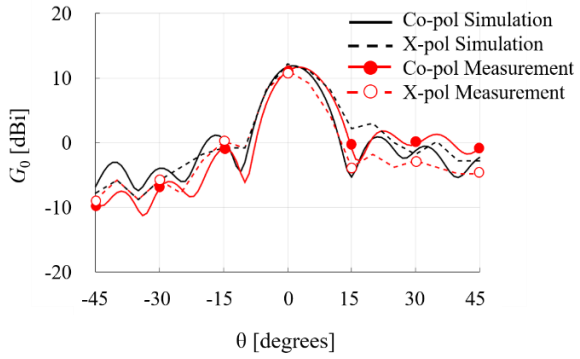

(a)

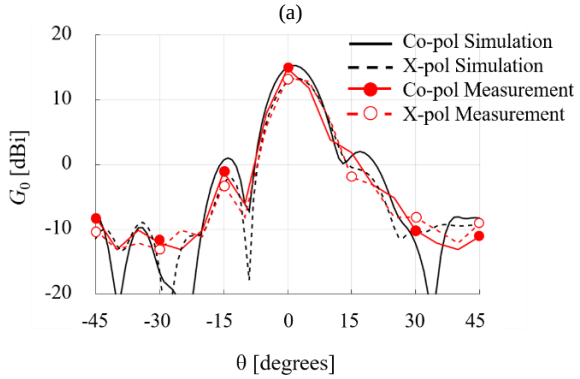

(b)

Fig. 11. Ultra-wideband, directive and circular polarization lens antenna radiation patterns. (a) f = 8 GHz, (b) f = 10 GHz.

TABLE 2. GAIN IN THE DIRECTION OF MAXIMUM RADIATION

f [GHz]	$G_{0\,(Simulation)}$ [dBi]		$G_{0\,(Measurement)}$ [dBi]	
	Co-pol	X-pol	Co-pol	X-pol
8.0	11.89	11.69	12.18	11.18
10	15.28	13.3	14.82	13.42

IV. CONCLUSION

This paper presented a high gain, ultra-wideband, circular polarization printed spiral antenna. The experimental results proved the efficiency of the structure, that could operate between 8.0 GHz to 15.6 GHz with gain up to 14.82 dBi. The proposed antenna is an interesting solution for future wireless communications that require high bandwidths, fast speeds, massive communication loads, over long distances.

ACKNOWLEDGMENT

The authors would like to acknowledge: UNIFEI's LabTel and LAIoI Groups, CAPES, CNPq, FAPEMIG (funding the RoboPatos Project APQ-02616-22), Inatel Competence Center, and the National Institute of Telecommunications – INATEL, Brazil.

REFERENCES

[1] G. H. Lee, S. Kumar, H. C. Choi and K. W. Kim, "Wideband High-Gain Double-Sided Dielectric Lens Integrated With a Dual-Bowtie Antenna," *in IEEE Antennas and Wireless Propagation Letters*, vol. 20, no. 3, pp. 293-297, March 2021, doi: 10.1109/LAWP.2020.3048165.

[2] W. Fu, E. R. Lopez, W. S. T. Rowe and K. Ghorbani, "A Planar Dual-Arm Equiangular Spiral Antenna," *in IEEE Transactions on Antennas and Propagation*, vol. 58, no. 5, pp. 1775-1779, May 2010, doi: 10.1109/TAP.2010.2044315.

[3] T. Pan, L. Dai, S. Chen, Z. Yan and Y. Lin, "Low-Impedance Flexible Archimedean-Equiangular Spiral Antenna," *in IEEE Antennas and Wireless Propagation Letters*, vol. 18, no. 9, pp. 1789-1793, Sept. 2019, doi: 10.1109/LAWP.2019.2930008.

[4] D. Chen, H. Zhang and J. Xu, "A Broadband Planar Spiral Antenna Design for Electromagnetic Signal Monitoring," *in IEEE Access*, vol. 8, pp. 73451-73456, 2020, doi: 10.1109/ACCESS.2020.2971135.

[5] X. Zhang, L. Zhu and Q. -S. Wu, "Sidelobe-Reduced and Gain-Enhanced Square Patch Antennas With Adjustable Beamwidth Under TM03 Mode Operation," *in IEEE Transactions on Antennas and Propagation*, vol. 66, no. 4, pp. 1704-1713, April 2018, doi: 10.1109/TAP.2018.2806220.

[6] X. Zhang, K. -D. Hong, L. Zhu, X. -K. Bi and T. Yuan, "Wideband Differentially Fed Patch Antennas Under Dual High-Order Modes for Stable High Gain," *in IEEE Transactions on Antennas and Propagation*, vol. 69, no. 1, pp. 508-513, Jan. 2021, doi: 10.1109/TAP.2020.3006394.

[7] R. A. Santos, G. L. S. Fré, L. G. Silva, M. C. Paiva, and D. H. Spadoti, "Ultra-Wideband Dielectric Lens Antennas for Beamsteering Systems," *in International Journal of Antennas and Propagation*, vol. 2019, Article ID 6732758, 8 pages, 2019, doi: 10.1155/2019/6732758

[8] G. H. Lee, S. Kumar, H. C. Choi and K. W. Kim, "Wideband High-Gain Double-Sided Dielectric Lens Integrated With a Dual-Bowtie Antenna," *in IEEE Antennas and Wireless Propagation Letters*, vol. 20, no. 3, pp. 293-297, March 2021, doi: 10.1109/LAWP.2020.3048165.

[9] R. Cicchetti, V. Cicchetti, A. Faraone, L. Foged and O. Testa, "A Compact High-Gain Wideband Lens Vivaldi Antenna for Wireless Communications and Through-the-Wall Imaging," *in IEEE Transactions on Antennas and Propagation*, vol. 69, no. 6, pp. 3177-3192, June 2021, doi: 10.1109/TAP.2020.3037777.

[10] U. Ullah, M. Al-Hasan, S. Koziel and I. B. Mabrouk, "Series-Slot-Fed Circularly Polarized Multiple-Input–Multiple-Output Antenna Array Enabling Circular Polarization Diversity for 5G 28 GHz Indoor Applications*," in IEEE Transactions on Antennas and Propagation*, vol. 69, no. 9, pp. 5607-5616, Sept. 2021, doi: 10.1109/TAP.2021.3066247.

[11] W. Fu, E. R. Lopez, W. S. T. Rowe and K. Ghorbani, "A Planar Dual-Arm Equiangular Spiral Antenna," *in IEEE Transactions on Antennas and Propagation*, vol. 58, no. 5, pp. 1775-1779, May 2010, doi: 10.1109/TAP.2010.2044315.

[12] V. H. Rumsey, "Frequency independent antennas: Technical Report no. 20." University of Ilinois, Urbana, 1957.

[13] C. A. Balanis, "Antenna theory: analysis and design", 3rd ed., John Wiley and Sons, Nova York, 2005.

[14] D. M. Pozar, "Microwave Engineering". 4th Ed. New York: John Willey, 2011.

[15] P. A. Rizzi, "Microwave Engineering: Passive Circuits", 1st Edition, Prentice-Hall, 1988.

[16] E. Huber, M. Mirzaee, J. Bjorgaard, M. Hoyack, S. Noghanian and I. Chang, "Dielectric property measurement of PLA," *in 2016 IEEE International Conference on Electro Information Technology (EIT)*, Grand Forks, ND, 2016, pp. 0788-0792.

[17] R. A. dos Santos, G. L. Fré and D. H. Spadoti, "Technique for constructing hemispherical dielectric lens antennas," *in Microwave and Optical Technology Letters*, 2019, doi: 10.1002/mop.31729.

Renan Alves dos Santos received the MSc in Telecomunication Engeneering from the National Institute of Telecommunications (Inatel), Brazil, in 2016 and PhD in Electrical Engineering from the Federal University of Itajubá (Unifei), Brazil, in 2019. Has been a professor at UFU in the Electronic and Telecommunications Engineering course at the Patos de Minas campus. His research focuses in electromagnetism applied to telecommunications (antennas, microwaves and wave propagation).

Gabriel Lobão Fré received the PhD in Electrical Engineering from Unifei – Federal University of Itajuba, and MSc in Telecommunication from Inatel – National Institute of Telecommunications. Is Telecommunication Engineer in R&D at Flextronics Institute of Technology (Fit), working in private applications of 5G-NR on industry 4.0 context since 2021. The areas of interest are radiocommunications, antennas and propagations, photonics and microwave, wireless communications networks architectures, IoT, 5G and 6G.

Danilo Henrique Spadoti graduated in electrical engineering from the University of Itajubá in 2002. He completed his master's degree in 2004 and his PhD in 2008 in electrical engineering, with a major in telecommunications at the University of São Paulo. In 2009, he did his postdoctoral studies abroad in Nanophotonics Group at Cornell University, Ithaca, USA. In 2010, he received a FAPESP postdoctoral scholarship from Mackenzie University. He is currently an associate professor in the area of telecommunications systems and applied electromagnetics at the Federal University of Itajubá.